International Journal of Heat and Mass Transfer 52 (2009) 4074–4081

Contents lists available at ScienceDirect

International Journal of Heat and Mass Transfer

journal homepage: www.elsevier.com/locate/ijhmt

Calculations of transport phenomena and reaction distribution in a polymer electrolyte membrane fuel cell

D.H. Schwarz, S.B. Beale *

National Research Council, Montreal Road, Ottawa, ON, Canada K1A 0R6

ARTICLE INFO

Article history:
Received 13 January 2009
Accepted 23 March 2009
Available online 13 May 2009

Keywords:
Fuel cells
Computational fluid dynamics
Electrochemistry
Transport phenomena
Chemical reactions
Physicochemical hydrodynamics
Current density

ABSTRACT

The performance of Polymer Electrolyte Membrane fuel cells depends on the design of the cell as well as the operating conditions. The design of the cell influences the complex interaction of activation effects, ohmic losses, and transport limitations, which in turn determines the local current density. Detailed models of the electrochemical reactions and transport phenomena in Polymer Electrolyte Membrane fuel cells can be used to determine the current density distribution for a given fuel cell design and operating conditions. In this work, three-dimensional, multicomponent and multiphase transport calculations are performed using a computational fluid dynamics code. The computational results for a full-scale fuel cell design show that ohmic effects due to drying of polymer electrolyte in the anode catalyst layer and membrane, and transport limitations of air and flooding in the cathode cause the current density to be a maximum near the gas channel inlets where ohmic losses and transport limitations are a minimum. Elsewhere in the cell, increased ohmic losses and transport limitations cause a decrease in current density, and the performance of the fuel cell is significantly lower than that which could be attained if the ohmic losses and transport limitations throughout the cell were the same as those near the gas channel inlets. Thus overall fuel cell design is critical in maximizing unit performance.

1. Introduction

Performance losses in Polymer Electrolyte Membrane (PEM) fuel cells depend on the design of the cell and the operating conditions. The cell design affects the complex interaction of activation, ohmic, and transport limitations. The resulting current density distribution is predominately influenced by variations in ohmic losses and transport limitations throughout the fuel cell.

Ohmic losses are primarily due to the conduction of protons in the polymer electrolyte of the catalyst layers and membrane. The polymer electrolyte needs to be well-hydrated in order to maximize the conductivity. A major problem with PEM fuel cells is maintaining hydration of the polymer electrolyte and, in order to reduce the water carried away by exiting gases due to evaporation, the reactant gas streams must be adequately humidified. However, at high current densities, transport of water from the anode to the cathode due to electro-osmotic drag occurs at a rate greater than that at which it can be restored by back diffusion from the cathode and through anode stream humidification. As a result, the polymer electrolyte tends to dry out in the anode catalyst layer and membrane. This decreases the electrical conductivity.

Transport limitations, which become dominant at high current densities, are primarily due to the use of air as the oxidant since the low concentration of oxygen in air and the accumulation of nitrogen lead to the formation of barriers for oxygen transport. Also, the rate at which oxygen can be supplied becomes limited by the production of water, which causes flooding. This effect is enhanced by electro-osmotic drag of water from the anode to the cathode. Flooding restricts gas transport, which causes the concentration of oxygen to decrease at catalyst sites, limiting the reaction rate.

Modeling studies provide a valuable tool for the investigation of the physicochemical phenomena occurring in PEM fuel cells. In this paper a comprehensive PEM fuel cell model is introduced and a computational implementation of the model for a specific fuel cell design is discussed. Finally, the model is used to investigate the effects of ohmic losses and transport limitations on current density distributions for the cell design.

2. Mathematical details

In this section a three-dimensional, multicomponent and multiphase model is presented for PEM fuel cells. In the anode and cathode gas channels and gas diffusion and catalyst layers the fundamental conservation laws are applied to the multicomponent gases [1]. The conservation of mass can be expressed in the form of the steady-state equation of continuity:

* Corresponding author.
E-mail address: steven.beale@nrc-cnrc.gc.ca (S.B. Beale).

0017-9310/$ - see front matter
doi:10.1016/j.ijheatmasstransfer.2009.03.043

Nomenclature

a	activity
c	concentration (kmol m^{-3})
C	condensation rate (s^{-1})
D	diffusion coefficient (m^2 s^{-1})
E	equivalent weight (kg kmol^{-1})
F	Faraday constant (9.6487×10^7 C kmol^{-1})
h	specific enthalpy (J kg^{-1})
i	current density (A m^{-2})
i_0	exchange current density (A m^{-2})
j	mass flux (kg m^{-2} s^{-1})
J	Leverett J-function
k	thermal conductivity (W m^{-1} K^{-1})
M	molecular weight (kg kmol^{-1})
P	pressure (Pa)
R	gas constant (8.3143×10^3 J kmol^{-1} K^{-1})
s	liquid water saturation
S	source (units of field variable $\times$ kg m^{-3} s^{-1})
T	temperature (K)
$\boldsymbol{u}$	velocity (m s^{-1})
V	voltage (V)
y	mass fraction

Greek symbols

α	transfer coefficient
β	concentration exponent
γ	surface tension (N m^{-1})
η	overpotential (V)
θ	contact angle (rad.)
κ	permeability (m^2)
λ	water content
μ	viscosity (kg m^{-1} s^{-1})
ξ	active surface area per unit volume (m^{-1})
ρ	density (kg m^{-3})
σ	electrical conductivity (S m^{-1})
τ	viscous stress (Pa)
ϕ	electrical potential (V)
φ	volumetric fraction

Superscripts

eff	effective
ref	reference

Subscripts

a	anodic
c	cathodic
f	fluid
i, j	species indices
m	membrane
n	species number
oc	open circuit
s	solid
sat	saturation
w	liquid water

$$\operatorname{div}(\rho \boldsymbol{u}) = \sum_{i=1}^{n} S_i \tag{1}$$

where the source terms are in general non-zero as a result of water phase changes and electrochemical reactions. Also, although the flow of gases is essentially incompressible, the mixture density is not constant because of variable gas composition, and is calculated from the ideal gas law for a multicomponent gas:

$$\rho = \frac{P}{RT\sum_{i=1}^{n} y_i/M_i} \tag{2}$$

The conservation of linear momentum for steady-state flow in the absence of external body forces (i.e. neglecting gravity) yields:

$$\operatorname{div}(\rho \boldsymbol{u} : \boldsymbol{u}) + \operatorname{grad} P + \operatorname{div} \boldsymbol{\tau} = -\frac{\mu}{\kappa}\boldsymbol{u} \tag{3}$$

and $\boldsymbol{u}$ is a superficial velocity. The term on the right-hand side of the equation is only significant in the porous gas-diffusion and catalyst layers and, when this term is large in comparison to the convection and viscous terms, Eq. (3) yields the incompressible form of Darcy's law [2]. Conversely when μ/κ is small the form of the Navier–Stokes equations are obtained. (NB: Though widely employed, the convection terms in Eq. (3) are not strictly correct for the intermediate condition, however, only the two limits were encountered in the present problem.)

Using the generalized Fick's law [3], neglecting thermal-diffusion (Soret effects) conservation of species may be written as

$$\operatorname{div}(\rho \boldsymbol{u} y_i) = \operatorname{div}\left(\rho \sum_j D_{ij}^{eff} \operatorname{grad}\ y_j\right) + S_i \tag{4}$$

The effective diffusion coefficients are given in terms of values at reference pressure and temperature by

$$D_{ij}^{eff} = [\varphi_f(1-s)]^{1.5} D_{ij}^{ref} \left(\frac{P^{ref}}{P}\right)\left(\frac{T}{T^{ref}}\right)^{1.75} \tag{5}$$

The pressure and temperature dependencies in Eq. (5) are from an empirical relation [4]. The dependencies on the porosity (i.e. volumetric fraction available for fluid flow) and liquid water saturation in the porous gas diffusion and catalyst layers take into account not only the volumetric fraction available for gas flow, but also the tortuosity of the porous media using effective medium theory [5].

For a binary gas there is only one independent Fick diffusion coefficient (namely the binary diffusion coefficient), such that for humidified hydrogen in the anode, $D_{11} = D_{H_2-H_2O}$. In contrast, say, for a ternary mixture, there are four independent Fick diffusion coefficients. For humidified air in the cathode, assuming a three-component gas and solving for the mass fractions of water vapor and oxygen in nitrogen, respectively, it can be shown that the Fick diffusion coefficient D_{11} is equal to the binary diffusion coefficient, $D_{H_2O-N_2}$, which arises from the fact that binary diffusion coefficient for water in oxygen and nitrogen, is the same. Also, the Fick diffusion coefficient, D_{22} is equal to the binary diffusion coefficient, $D_{O_2-N_2}$, to within 2%, since the diffusion of oxygen is predominately through nitrogen. Finally it can be shown that D_{12} and D_{21} are small compared to D_{11} and D_{22} (i.e. less than 6%) and can justifiably be neglected. Thus, based on an order-of-magnitude analysis, the use of Fick's law is justified.

Neglecting the effects of kinetic energy convection, enthalpy diffusion (Dufour effects) and viscous dissipation, conservation of energy for steady-state flow yields

$$\operatorname{div}(\rho \boldsymbol{u} h) = \operatorname{div} k^{eff} \operatorname{grad} T + S_h \tag{6}$$

where the source term takes into account local heat production due to water phase changes, ohmic resistances, activation overpotentials and heat of reaction. In Eq. (6) the effective thermal conductivity takes into account the conductivity of both the solid and fluid phases for flow in porous media, assuming that local thermal equilibrium applies.

The electric field potentials associated with electron and proton conduction are given by

$$\operatorname{div}(\sigma_s^{eff}\operatorname{grad}\phi_s)+S_s=0 \tag{7}$$

$$\operatorname{div}(\sigma_m^{eff}\operatorname{grad}\phi_m)+S_m=0 \tag{8}$$

where the overall or net sources must be equal and opposite. In Eq. (8) a fit to experimental data for Nafion® 117 conductivity [6] is used:

$$\sigma_m^{eff}=\varphi_m^{1.5}e^{1268\left(\frac{1}{303}-\frac{1}{T}\right)}\begin{cases}0.5139\lambda-0.326, & \lambda>1\\ 0.1879, & \lambda\leqslant 1\end{cases} \tag{9}$$

Eq. (9) takes into account the effective conductivity in the catalyst layers as a function of volumetric fraction and tortuosity using the effective medium theory. Also, in the catalyst layers the water content in the polymer electrolyte (concentration of water divided by concentration of fixed negative charge sites) is related to the activity of water in the adjacent pores using an experimentally derived relationship [6] for Nafion® 117:

$$\lambda=\begin{cases}0.043+17.81a-39.85a^2+36a^3, & 0\leqslant a\leqslant 1\\ 14+1.4(a-1), & 1<a\leqslant 3\end{cases} \tag{10}$$

In Eq. (10) the activity is given in terms of the water vapor partial pressure, saturation pressure and liquid water saturation by [7]

$$a=\frac{P_{H_2O}}{P_{sat}}+2s \tag{11}$$

The mass flux of liquid water in the membrane due to electro-osmotic drag and diffusion, is given by [6]

$$\boldsymbol{j}_m=\left(\frac{2.5}{22}\right)M_{H_2O}\frac{\boldsymbol{i}_m}{F}\lambda-\frac{\rho_{dry}}{E_{dry}}M_{H_2O}D_m\operatorname{grad}\lambda \tag{12}$$

In Eq. (12) a fit [8] to experimental data for Nafion® 117 [6] is used for the diffusion coefficient:

$$D_m=10^{-10}\times e^{2416\left(\frac{1}{303}-\frac{1}{T}\right)}\times\begin{cases}1, & \lambda<2\\ 1+2(\lambda-2), & 2\leqslant\lambda\leqslant 3\\ 3-1.167(\lambda-3), & 3<\lambda<4.5\\ 1.25, & \lambda\geqslant 4.5\end{cases} \tag{13}$$

The mass flux of liquid water in the gas channels and gas diffusion and catalyst layers is given by

$$\boldsymbol{j}_w=\rho_w s\boldsymbol{u}-\rho_w\frac{s^3\kappa}{\mu_w}\frac{d}{ds}\left[\frac{\gamma\cos\theta}{(\kappa/\varphi_f)^{1/2}}J\right]\operatorname{grad}s \tag{14}$$

The second term on the right-hand side of Eq. (14) is derived from Darcy's law and applies only to the porous gas diffusion and catalyst layers. In general, gas and liquid water pressures differ by the capillary pressure. However, changes in gas pressure are relatively small in PEM fuel cells such that changes in liquid water pressure are mainly due to changes in capillary pressure. Capillary pressure is given in terms of the Leverett J-function [9], which is only a function of liquid water saturation, by the expression in the square brackets in Eq. (14). Also the permeability of the porous media to liquid water is assumed to be given by $s^3\kappa$ [5]. The effects of liquid water in the gas channels are not considered here.

Instead it is assumed that water from the gas diffusion layers which reaches the channels is simply transported out of the channels at the same velocity as the gases. Neglecting Darcy's law in Eq. (14) yields the resulting convective term for the gas channels. In the PEM fuel cell model, changes in liquid water mass flux, $\boldsymbol{j}_w$, are considered to be only due to water phase changes as given by Eq. (17) below.

Reaction rates in the anode and cathode catalyst layers are prescribed by the Butler–Volmer equations [10]:

$$\begin{aligned}S_{s,a}&=\xi i_{0,a}^{ref}\left(\frac{c_{H_2}}{c_{H_2}^{ref}}\right)^{\beta_a}\left(e^{-\alpha_{c,a}\eta_a F/RT}-e^{\alpha_{a,a}\eta_a F/RT}\right)\\ S_{s,c}&=\xi i_{0,c}^{ref}\left(\frac{c_{O_2}}{c_{O_2}^{ref}}\right)^{\beta_c}\left(e^{-\alpha_{c,c}\eta_c F/RT}-e^{\alpha_{a,c}\eta_c F/RT}\right)\end{aligned} \tag{15}$$

The overpotentials driving the electrochemical reactions in Eq. (15) are related to potential differences between the solid and polymer electrolyte phases in the anode catalyst layer by $\eta_a=\phi_s-\phi_m$ and in the cathode catalyst layer by $\eta_c=\phi_s-\phi_m-V_{oc}$ [11]. The open circuit voltage is given in terms of the reversible potential by the Nernst equation. However, the open circuit voltage departs from its reversible value due to competing reactions which set up a mixed potential and as a result, an experimental value [12] is used instead.

The non-zero terms in Eqs. (1) and (4) for the electrochemical reactions in the anode and cathode catalyst layers, are given by

$$\begin{aligned}S_{H_2}&=\frac{M_{H_2}}{2F}S_{s,a}\\ S_{O_2}&=-\frac{M_{O_2}}{4F}S_{s,c}\\ S_{H_2O}&=\frac{M_{H_2O}}{2F}S_{s,c}-S_w-\operatorname{div}\boldsymbol{j}_m\end{aligned} \tag{16}$$

In Eq. (16), the $\boldsymbol{j}_m$ term is due to water uptake/transport through the membrane and the S_w term is due phase change in the diffusion and catalyst layers [5,13]:

$$S_w=C\max\left\{(1-s)\frac{P_{H_2O}-P_{sat}}{RT}M_{H_2O},-s\rho_w\right\} \tag{17}$$

and the terms in parenthesis are due to condensation or evaporation, respectively.

In order to obtain practical engineering solutions, the governing system of coupled non-linear partial differential equations are converted to systems of linear algebraic equations by means of well-established finite-volume techniques [14]. A computer code may then be readily employed to obtain numerical solutions for any given fuel cell design. In this program of research, a version of the FLUENT™ code [15] was modified for implementation of the model equations, for the specific geometry detailed below.

3. Fuel cell prototype

The PEM fuel cell model is implemented and a model prototype constructed for a full-scale fuel cell design, currently under development. Fig. 1 shows a schematic of the design. On the anode side, a multi-pass serpentine arrangement of twin gas channels with 46 bends (23 per side), width and height of 1.2796×10^{-3} m, and

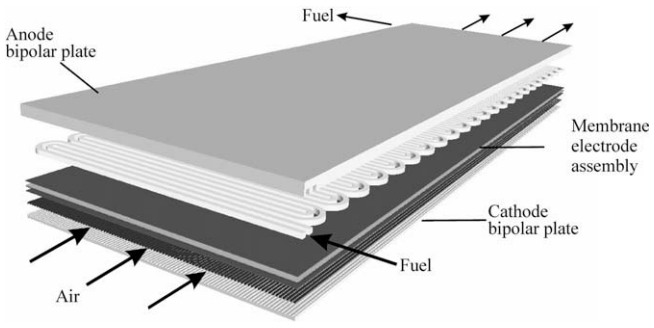

Fig. 1. Schematic of fuel cell prototype considered in this study.

lengths of 3.649 m, land widths 1.2736×10^{-3} m, provides fuel to the cell. On the cathode there are 93 straight (i.e. single-pass) gas channels with widths and heights of 3.656×10^{-4} m, lengths of 0.24 m and land widths between gas channels of 5.0×10^{-4} m.

Operating conditions for the PEM fuel cell implementation include constant mass flow rates at the anode and cathode gas channel inlets corresponding to a stoichiometric number of 3 at mean current density of 1 A cm^{-2} (10,000 A m^{-2}). Co-flow of hydrogen and air at 100% relative humidity and temperatures of 70 °C are assumed at the inlets. Back pressures of 3 atm (3.04 bar) are applied at the gas channel outlets in both the anode and cathode.

The domain was tessellated with a grid consisting of nominally eighteen million computational cells, which was used to perform all the computations presented in this paper. This mesh was the maximum size that could be handled with the available computing equipment, namely a 32-node beowulf cluster with an aggregate memory of 256 GByte. Further grid refinement studies could not therefore be entertained on this equipment. In the cathode and membrane electrode assembly regions, a structured hexahedral mesh was employed, whereas on the anode-side an unstructured mesh, fitted to the serpentine passage, was utilized. Fig. 2 shows the meshes employed in the two regions. At the non-conformal interface between the two sub-domains tri-linear interpolation was employed to convert primitive variables and fluxes, as necessary. Parameters associated with the CFD implementation of the PEM fuel cell model are given fixed values at the stated operating conditions from published results, which have been determined by separate experimental measurements. Further values for the model parameters are provided in refs. [16,17]. Besides the operating conditions and model parameters, properties of the PEM fuel cell components are required. The other components in the fuel cell are the (i) bipolar plates; made of SGL BBP4 carbon/phenolic composite, (ii) Toray TGP-H-060 gas diffusion layers and (iii) Gore Primea® Series 5510 catalyst-coated composite membrane. Properties of these components as supplied by the manufacturers [16,17] were used in the performance calculations.

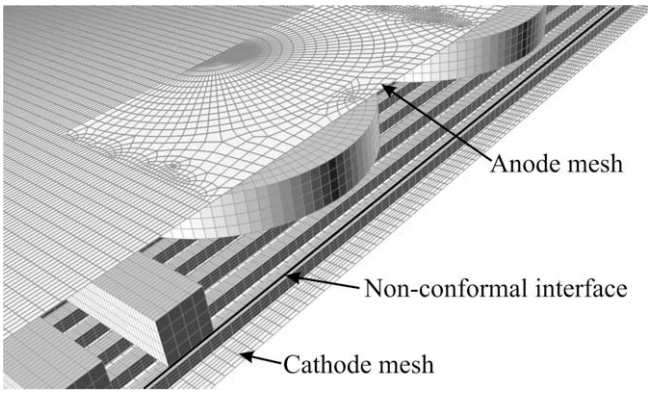

Fig. 2. Details of non-conformal mesh.

4. Analysis of results

Fig. 3 shows CFD results for water vapor concentration in the anode catalyst layer at a current density of 1 A cm^{-2} (10,000 A m^{-2}). The water vapor concentration in the anode decreases along the serpentine gas channels and under the bipolar plates between the channels as can been seen from the pattern in Fig. 3. The concentration also decreases from the gas channels through the gas diffusion layer to the catalyst layer. These results are due to electro-osmotic drag transporting water through the membrane from the anode to the cathode. Also, the water vapor concentration decreases with increasing current density since electro-osmotic drag increases with current density. In contrast, although water is produced in the cathode and is transported by electro-osmotic drag from the anode to the cathode, water vapor concentration in the cathode is found to be relatively constant since it is limited by the formation of liquid water to its fully saturated value.

Fig. 4 is similar to Fig. 3, except that it shows hydrogen concentration in the anode catalyst layer at a current density of 1 A cm^{-2} (10,000 A m^{-2}). The decrease in water vapor concentration along the serpentine gas channels and under the bipolar plates between the channels, as shown in Fig. 3, causes a corresponding increase in hydrogen concentration (as can been seen from the pattern in Fig. 4). However, because the concentration of hydrogen is large

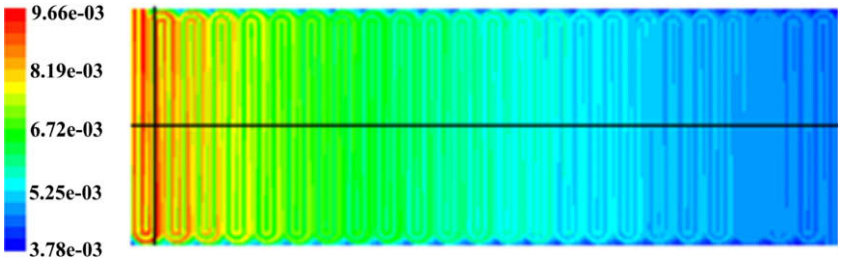

Fig. 3. Water vapor concentration in anode catalyst layer (kmol m^{-3}).

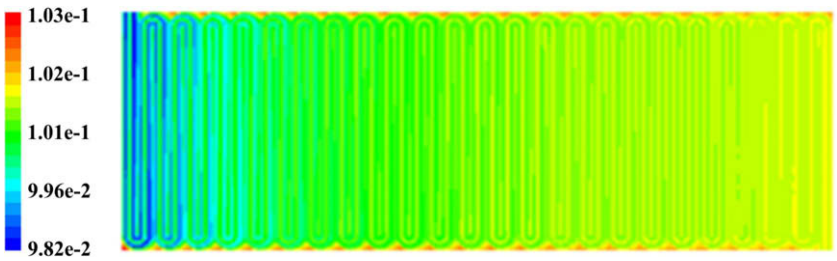

Fig. 4. Hydrogen concentration in anode catalyst layer (kmol m^{-3}).

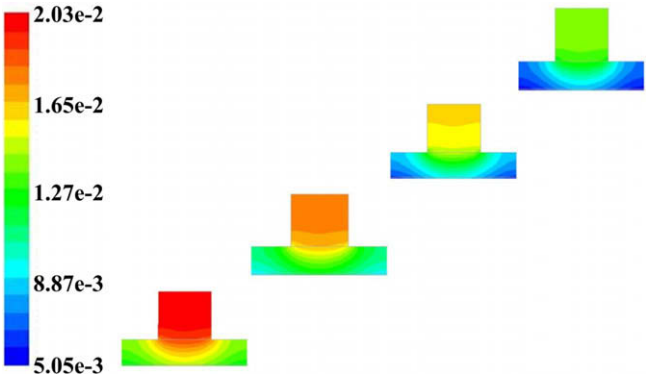

Fig. 5. Oxygen concentration in cathode gas channel and gas diffusion and catalyst layers (kmol m^{-3}).

compared to that of water vapor, the relative increases in hydrogen concentration are much smaller. Thus, even though electro-osmotic drag increases with current density, causing larger decreases in water vapor mole fraction and corresponding increases in hydrogen concentration, the changes in hydrogen concentration are relatively small.

Fig. 5 shows oxygen concentration in the center cathode gas channel and underlying parts of the gas diffusion and catalyst layers at a current density of 1 A cm^{-2} (10,000 A m^{-2}) for slices separated by equal lengths along the channel from near the inlet at the lower left to near the outlet at the upper right. The results of Fig. 5 show that the concentration decreases from the gas channel through the diffusion layer to the catalyst layer, and under the bipolar plate because of the longer diffusion length scale, and towards the gas channel outlet because of oxygen consumption. As shown in Fig. 5, the minimum concentration varies significantly from the concentration near the gas channel inlet. The minimum is also found to decrease substantially with current density. Thus the results show the expected decrease in oxygen concentration associated with the transport resistances of air and liquid water, which increase as the current density increases, causing large transport limitations at high current densities.

Fig. 6 shows liquid water saturation in the cathode catalyst layer at a current density of 1 A cm^{-2} (10,000 A m^{-2}). As shown in Fig. 6, the distribution of liquid water in the cathode depends on production and water transport from the anode with saturation increasing towards the gas channel outlets as more water is carried away in the gas channels. The saturation also increases through the gas diffusion layer from adjacent to the gas channels to adjacent to the catalyst layer and under the bipolar plate. Flooding is found to increase as current density increases, with liquid water saturation restricting the mass transport of oxygen causing transport limitations. Note that there is no liquid water in the anode because the water vapor concentration shown in Fig. 3 is below the fully saturated value.

Fig. 7 shows polymer electrolyte water content in the membrane and anode and cathode catalyst layers along the horizontal and vertical lines as shown in Fig. 3 at a current density of 1 A cm^{-2} (10,000 A m^{-2}). The horizontal line in Fig. 3 is under the central cathode gas channel and the vertical line is under the bipolar plate between the two anode gas channels near the inlets and crosses bends of the channels near the bottom and top. As shown in Fig. 7(a) and (b), water content decreases from the cathode catalyst layer through the membrane to the anode catalyst layer. Fig. 7(a) also shows that water content decreases under the anode bipolar plates and towards the gas channel outlet in the membrane and

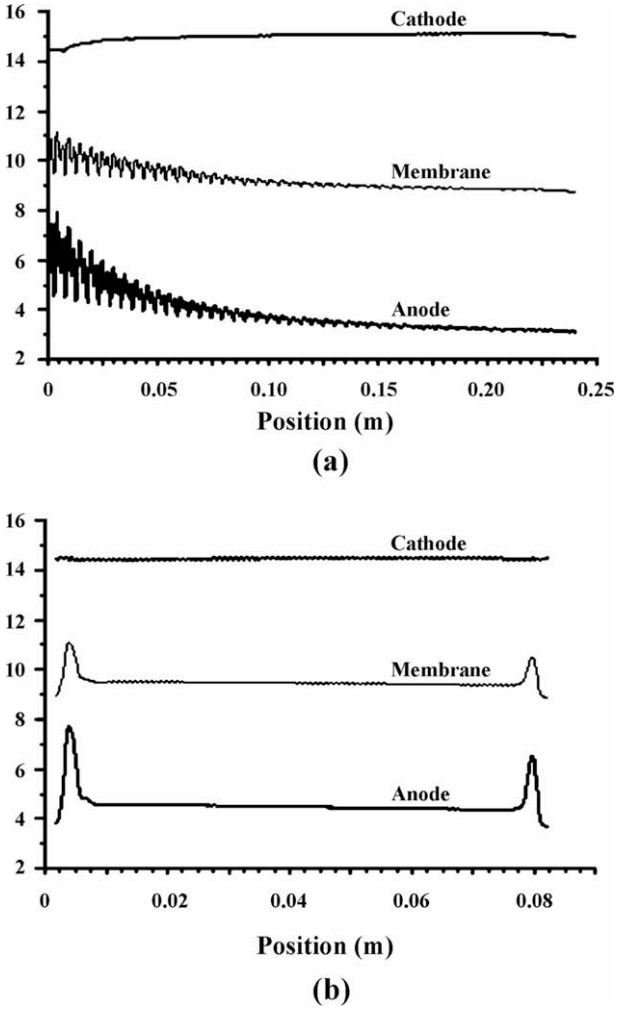

Fig. 7. Water content in membrane and anode and cathode catalyst layers (a) under the length of the central cathode gas channel and (b) perpendicular to the cathode gas channels near the inlets.

Fig. 6. Liquid water saturation in cathode catalyst layer.

anode catalyst layer. In contrast, water content increases slightly towards the gas channel outlet in the cathode catalyst layer due to increasing liquid water saturation. Fig. 7(b) shows a corresponding increase in water content under the anode gas channels in the membrane and anode catalyst layer. The water content in the anode catalyst layer and membrane decreases with current density and, as indicated in Fig. 7, at a current density of 1 A cm^{-2} (10,000 A m^{-2}) the anode catalyst layer and membrane are already quite dry. The decrease in protonic conductivity due to drying of the polymer electrolyte is substantial, causing large ohmic losses in the anode catalyst layer and membrane.

Fig. 8 shows overpotential in the anode catalyst layer at a current density of 1 A cm^{-2} (10,000 A m^{-2}). The patterns in Fig. 8(a) and (b) are similar to those seen in Fig. 3, which indicates that the distribution of overpotential in the anode catalyst layer is determined by the water vapor concentration. This is because water vapor concentration determines polymer electrolyte water content which in turn determines protonic conductivity. The ohmic losses due to low protonic conductivity in the anode catalyst layer and membrane cause a decrease in local current density and a corresponding decrease in overpotential. Fig. 8(a) and (b) also show that overpotential is higher near to the membrane than near the gas diffusion layer.

Fig. 9 shows local reaction rate in the anode catalyst layer at an average current density of 1 A cm^{-2} (10,000 A m^{-2}). The patterns in Fig. 9(a) and (b) are similar to those seen in Fig. 8(a) and (b), which indicates that the distribution of reaction rate in the anode catalyst layer is determined by the overpotential. This is because changes in hydrogen concentration are relatively small (as shown in Fig. 4) so that changes in reaction rate are completely determined by the overpotential. Fig. 9(a) and (b) shows that reaction rate is much higher adjacent to the membrane than to the gas

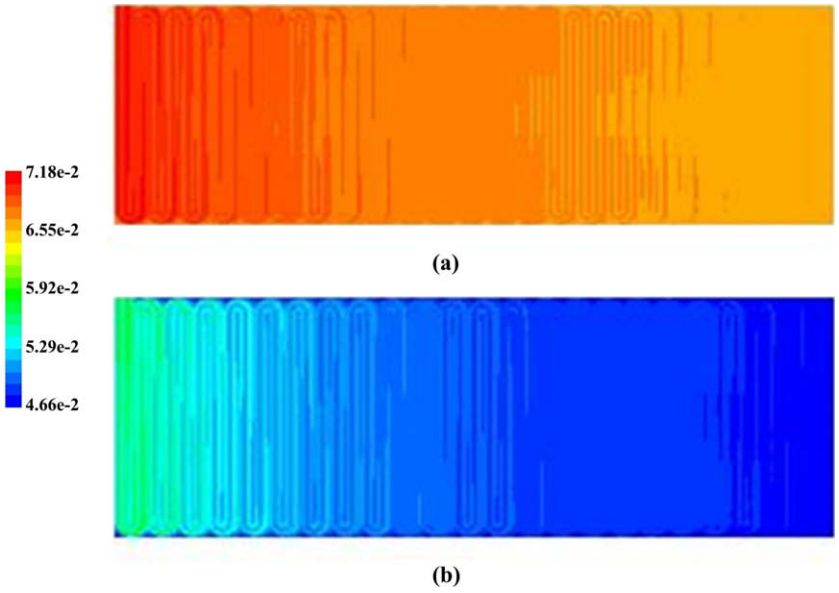

Fig. 8. Overpotential in anode catalyst layer adjacent to (a) membrane and (b) gas diffusion layer (V).

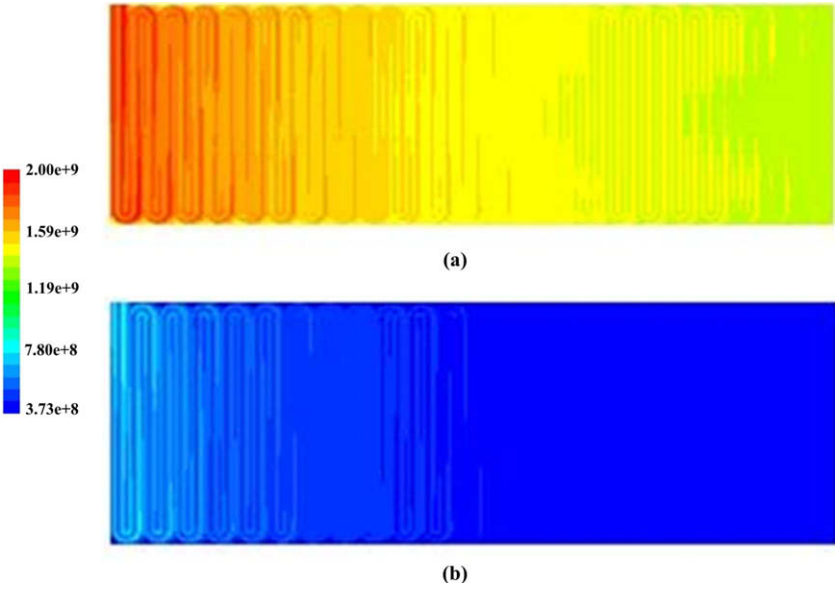

Fig. 9. Reaction rate in anode catalyst layer adjacent to (a) membrane and (b) gas diffusion layer (A m^{-3}).

diffusion layer. Reactions are concentrated near the anode gas channel inlets, where the high water vapor concentrations yield high polymer electrolyte water content and low ohmic losses.

Fig. 10 shows reaction rate in the cathode catalyst layer along the horizontal and vertical lines shown in Fig. 1 at a current density of 1 A cm^{-2} (10,000 A m^{-2}). As shown in Fig. 10(a), reaction rate decreases under the anode bipolar plates due to low water vapor concentrations yielding low polymer electrolyte water content and high ohmic losses. Reaction rate also decreases towards the cathode gas channel outlet due to decreasing oxygen concentration. Fig. 10(b) shows a corresponding increase in reaction rate under the anode gas channels and also a decrease along the channel lengths. Fig. 10(a) and (b) shows that reactions are concentrated near the cathode gas channels inlets, where oxygen concentration is high and near the anode gas channel inlets where high polymer electrolyte water content yields low ohmic losses. However, the cathode reactions are not as concentrated as those in the anode.

Figs. 9 and 10 together show that reactions are concentrated near the gas channel inlets where ohmic losses and transport limitations are minimized. The variations in reactions are already quite large at a current density of 1 A cm^{-2} (10,000 A m^{-2}) and the variations become even larger as current density increases. Thus the results show that for the design of Fig. 1, performance of the fuel cell is much lower than that which could be attained if the ohmic losses and transport limitations throughout the cell were the same as those near the gas channel inlets. Thus fuel cell performance would be significantly increased by new designs aimed at minimizing the ohmic losses and transport limitations elsewhere in the fuel cell, not only at the gas inlets. This observation reinforces the utility of the role of mathematical modeling in making the transition from small-scale fuel cells to industrial designs where macroscopic (i.e. continuum) effects can significantly degrade performance.

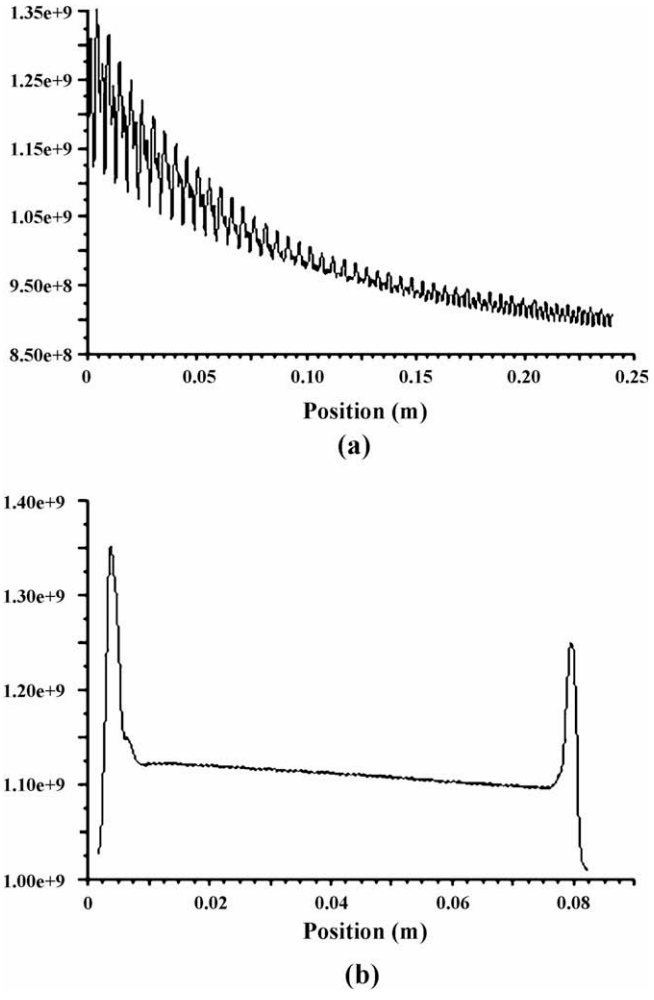

Fig. 10. Reaction rate in the cathode catalyst layer (a) under the length of the central cathode gas channel and (b) perpendicular to the cathode gas channels near the inlets (A m^{-3}).

5. Conclusion

In this paper, results are presented for a three-dimensional, multicomponent and multiphase model of a PEM fuel cell. The effects of ohmic losses and transport limitations are explored and the CFD computations show that drying of the polymer electrolyte in the anode catalyst layer and membrane causes the current density in the anode catalyst layer to be concentrated near the anode gas channel inlets. The CFD results also show that resistances to the transport of oxygen by air and flooding cause the current density in the cathode catalyst layer to be concentrated near the cathode gas channel inlets. Thus ohmic losses and transport limitations play an important role in determining current density distributions, which in turn are a measure of the effectiveness of the PEM fuel cell design at attaining maximum performance. Therefore the effects of ohmic losses and transport limitations on current density distributions should be an important consideration in the design of PEM fuel cells.

Acknowledgements

Prof. D.B. Spalding's seminal contributions to computational fluid dynamics, and his introduction to one of the authors (SB) of the subject of physicochemical hydrodynamics many years ago, have significantly influenced the work presented here and elsewhere. The authors would also like to thank the following individuals (in alphabetical order) for their support in this project; M. Blanco, E. Gu., R. Jerome, J. Martin, H. Wang, X.-Z. Yuan.

References

[1] R.B. Bird, W.E. Stewart, E.N. Lightfoot, Transport Phenomena, second ed., Wiley, New York, 2001.
[2] D.A. Nield, A. Bejan, Convection in Porous Media, second ed., Springer, New York, 1999.
[3] R. Taylor, R. Krishna, Multicomponent Mass Transfer, Wiley/Interscience, New York, 1993.
[4] E.L. Cussler, Diffusion: Mass Transfer in Fluid Systems, second ed., Cambridge University Press, Cambridge, 1997.
[5] J.H. Nam, M. Kaviany, Effective diffusivity and water-saturation distribution in single- and two-layer PEMFC diffusion medium, Int. J. Heat Mass Transfer 46 (2003) 4595–4611.
[6] T.E. Springer, M.S. Wilson, S. Gottesfeld, Modeling and experimental diagnosis in polymer electrolyte fuel cells, J. Electrochem. Soc. 140 (1993) 3513–3526.
[7] B.M. Eaton, One dimensional, transient model of heat, mass, and charge transfer in a proton exchange membrane, M.Sc. Thesis, Virginia Polytechnic Institute and State University, 2001.
[8] S. Dutta, S. Shimpalee, J.W. Van Zee, Numerical prediction of mass-exchange between cathode and anode channels in a PEM fuel cell, Int. J. Heat Mass Transfer 44 (2001) 2029–2042.
[9] M.C. Leverett, Capillary behavior in porous solids, AIME Trans. 142 (1941) 152–169.
[10] J.O.M. Bockris, S.U.M. Khan, Surface Electrochemistry: A Molecular Level Approach, Plenum Press, New York, 1993.
[11] S. Um, C.-Y. Wang, K.S. Chen, Computational fluid dynamics modelling of proton exchange membrane fuel cells, J. Electrochem. Soc. 147 (2000) 4485–4493.
[12] A. Parathasarthy, S. Srinivasan, A.J. Appleby, C.R. Martin, Temperature dependence of the electrode kinetics of oxygen reduction at the platinum/

nafion® interface – a miroelectrode investigation, J. Electrochem. Soc. 139 (1992) 2530–2537.
[13] D. Natarajan, T.V. Nguyen, A two-dimensional, two-phase, multicomponent, transient model for the cathode of a proton exchange membrane fuel cell using conventional gas distributors, J. Electrochem. Soc. 148 (2001) A1324–A1335.
[14] S.V. Patankar, Numerical Heat Transfer and Fluid Flow, Hemisphere, New York, 1980.
[15] S. Li, U. Becker, A Three Dimensional CFD Model for PEMFC, Fluent Inc., Lebanon, New Hampshire, 2004.
[16] D.H. Schwarz, Modelling catalyst layers in pem fuel cells: effects of transport limitations and non-uniform platinum loading, M.A.Sc. Thesis, University of Victoria, Vic., BC, 2005.
[17] D.H. Schwarz, S.B. Beale, Diagnostic modelling fuel cell – CFD modelling, PET-1576-08S, National Research Council, Ottawa, 2008.